Extraction of the Hepatic Vasculature in Rats Using 3D Micro-CT Images

Shu-Yen Wan, *Member, IEEE*, Atilla P. Kiraly, Erik L. Ritman, and William E. Higgins, *Senior Member, IEEE*

Abstract

High-resolution micro–CT scanners now exist for imaging small animals. In particular, such a scanner can generate very large three-dimensional (3D) digital images of the rat's hepatic vasculature. These images provide data on the overall structure and function of such complex vascular trees. Unfortunately, human operators have extreme difficulty in extracting the extensive vasculature contained in the images. Also, no suitable tree representation exists that permits straightforward structural analysis and information retrieval. This work proposes an automatic procedure for extracting and representing such a vascular tree. The procedure is both computation and memory–efficient and runs on current PCs. As results demonstrate, the procedure faithfully follows human-defined measurements and provides far more information than can be defined interactively.

Keywords

micro–CT imaging, small–animal imaging, 3D image processing, 3D image analysis, region growing, angiography, hepatic imaging, liver, virtual endoscopy.

I. INTRODUCTION

Standard radiologic imaging techniques, such as PET, MRI, and CT, have been adapted recently to the imaging of small animals [1–7]. High resolution imaging of small animals admits the possibility of controlled studies of disease phenotype and of micro-organ structure and function. In particular, newly devised high-resolution micro-CT scanners generate three-dimensional (3D) images of sufficient resolution and specimen size (large enough to encompass an intact small-rodent organ) to provide data on an organ's in situ basic functional units (BFUs). A BFU, defined as the smallest anatomical unit that functions as an organ (e.g., the hepatic lobule), can have a volume on the order of 0.1 mm^3 [4,8,9]. Existing micro-CT scanners, which give voxel resolution on the order of 2-30 μm, allow examination of the hierarchical microarchitecture of the vasculature of organ BFUs, including their in situ geometry and packing.

A typical digitized micro-CT image of a rat hepatic lobule has a size of 100MB or more. While the resolution of the vasculature is spectacular, the image's enormous size introduces three challenges. First, the standard image-analysis procedure requires hours of human interaction to identify a single vascular branch [9]. This is far too time consuming to permit extensive extraction of a more complete vascular network [10]. Other drawbacks, such as limited reproducibility and the laborious task involved in doing true 3D analysis, also hamper this procedure's efficacy. As a second challenge, computerized automatic processing of a large image demands considerable amounts of storage space, processing memory, and computational complexity. An existing image-analysis system contains a semi-automatic module for extracting bright vasculature trees from a 3D image [9,11]. But its segmentation scheme, thresholding, is sensitive to artifactual variations in gray scale and does not consider connectivity of regions making up a tree. The third challenge to analyzing micro-CT images of the vasculature is the need for an efficient vascular-tree representation.

Dr. S.-Y. Wan is with the Department of Information Management, Chang Gung University, Taiwan, R.O.C., E-mail: wan@cse.psu.edu.
Mr. A.P. Kiraly is with the Department of Computer Science and Engineering (CSE), Penn State University, E-mail: kiraly@cse.psu.edu.
Dr. E.L. Ritman is with the Department of Physiology and Biophysics, The Mayo Clinic and Foundation, E-mail: elran@mayo.edu.
Dr. W.E. Higgins is with the Departments of Electrical Engineering, CSE, and Bioengineering, Penn State University, E-mail: weh2@psu.edu.

Such a representation is necessary for efficient retrieval and analysis of a tree's structure, and it assists in visualization.

To address these challenges, we propose an efficient procedure for extracting and representing the vasculature of the hepatic vascular system contained in micro–CT images. The procedure, inspired by a recently proposed system for 3D angiographic analysis [12], is largely automatic and gives reproducible results. It employs a new 3D region growing technique that is fast, memory–efficient, and relatively insensitive to starting conditions [13, 14]. The region growing technique is also used for efficient deletion of interior cavities of the vascular network. Further, the complete procedure employs a compact tree-representation scheme that permits rapid branch pruning, network reorganization, and information retrieval. Section II of this paper describes the experimental protocol used in our efforts. Section III presents the proposed procedure. Section IV presents validation results for several micro-CT images of the blood supply of rat hepatic lobes. Finally, Section V offers concluding remarks.

II. EXPERIMENTAL PROTOCOL

The rat was anesthetised and the ascending aorta exposed after a thoracotomy. After intravenous injection of heparin, the rat was euthanised with an intravenous injection of pentobarbital. Next, the aorta was cannulated and flushed with saline, following which microfil (containing lead chromate) was infused at 100 mm Hg until it appeared in the right ventricle. The aorta was ligated, and the animal placed in refrigerator overnight to permit the microfil to set. The next morning, the liver was removed and dehydrated with a sequence of immersions in glycerol of increasing concentrations. Following this, the liver was fixed in bioplastic.

Next, the specimen was placed on top of a computer–controlled rotation stage in the micro-CT scanner. The scanner is described in detail in [4]. In brief, it consists of a spectroscopy X–ray source that generates X–ray photons of a nominal 18 keV energy. The X–rays transmitted through the specimen expose a crystalline plate of cesium iodide (doped with thallium) which converts the X–ray image to a light image. This image is focused onto a CCD detector array (1024×1024 square pixels, each 21 μm on a side) with a microscope objective operated at 1:1 or 1:4 magnification. The specimen is rotated in 0.5 degrees around 360 degrees about its vertical axis in between each X–ray exposure. The recorded X–ray projection gray scale was then converted to logarithmic values and a modified Feldkamp cone beam tomographic reconstruction performed. The resulting 3D image has cubic voxels, with each voxel being 21 μm on a side. Each voxel has 16 bits of gray scale information.

III. ANALYSIS PROCEDURE

A. Image Characteristics

Our goal is to extract the vascular tree of the hepatic system and provide a complete geometric description of the extracted tree. Fig. 1 shows 2D coronal (x–z) maximum–intensity projections (MIPs) for three of the 3D micro-CT images used in this paper. Six characteristics are common to these images. First, the vascular tree appears brighter than the background in the acquired images. Second, voxels at the middle of the larger proximal vessels may appear dimmer than the other tree voxels. This occurs because of the fall-off in the imaging system's modulation transfer

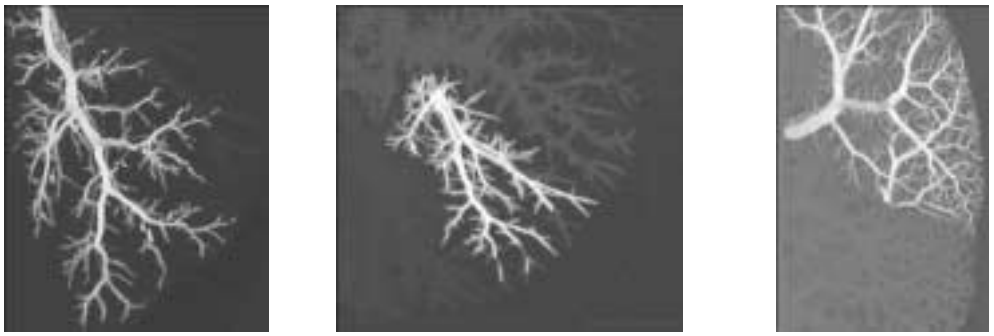

(a) *control1* (80.2 MB) Dimensions: $399 \times 215 \times 491$ (b) *control2* (114.4 MB) Dimensions: $400 \times 400 \times 375$ (c) *control3* (73 MB) Dimensions: $319 \times 247 \times 487$

Fig. 1. Coronal maximum-intensity projection (MIP) images for three 3D micro-CT images. Each original 3D image depicts a single hepatic lobule of a rat liver, where the bile ducts were first selectively opacified with a contrast agent before scanning. The digital image dimensions are given for each image. The voxel size has $\Delta x = \Delta y = \Delta z = 21\mu$m for all cases.

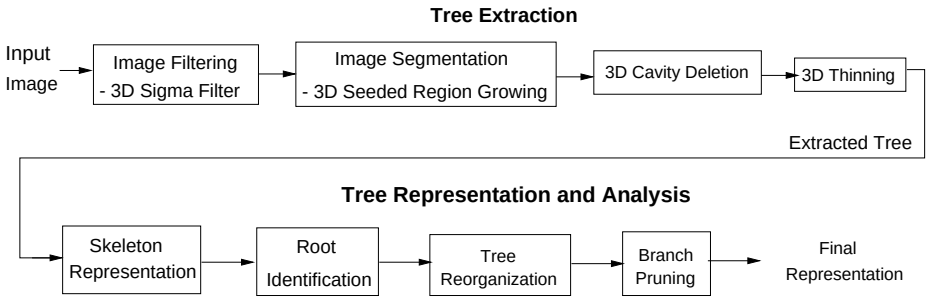

Fig. 2. Micro–CT image-analysis procedure. The first stage defines regions of interest. The second stage defines the vascular tree representation and quantitative data.

function and X–ray beam hardening artifact. Third, intensity values along the tree may vary due to the contrast medium's inconsistent spreading. Fourth, the root, or starting point, of the vascular tree may occur at any location within the image (e.g., per Figure 1, the root of *control1* is at the top left of the image, whereas the root of *control3* is to the left and center of the image) and the outer zones of the 3D image tends to be less contrast than the central region. Fifth, the usual degradations of tomographic images arise from reconstruction (streak) artifacts, noise, and partial–volume averaging. Finally, the images are very large, ranging in size from 73 MB to 114 MB in this study. From these characteristics, we can surmise that a suitable processing procedure, must be memory efficient, overcome intensity variations and degradations of the tree, and provide a means for identifying the root vessel.

B. Procedure Overview

Fig. 2 depicts the proposed procedure. The well known *3D sigma filter* ($3\times3\times3$ mask, $\sigma = 10$) is first applied to reduce image noise, sharpen regions, preserve edges and retain thin branches [12]; it especially helps make the subsequent region-based segmentation be more robust. A new *3D seeded–region–growing* segmentation scheme is then performed on the filtered image to extract the raw regions of interest [13–15]. *3D cavity deletion* is next applied to fill possible erroneous interior tree cavities contained in the segmented result. Next, we use the *3D homotopy–preserving thinning* algorithm of Saha *et al.* to define the central axes (or skeleton) of the segmented network [16].

At this point, a complete thinned tree exists. This tree, however, demands excessive computer storage space, especially considering that it typically contains >95% background voxels (0s). Further, it gives no information on the tree's geometry or quantitative characteristics. Our proposed tree representation alleviates this burden. Four steps are involved in building this representation: *skeleton representation*, to convert the raw 3D image of the skeleton into a compact voxel list made up only of skeleton voxels; *root identification*, to specify the tree's root branch; *tree reorganization*, to reorder the tree's representation so that the identified root branch starts the tree; and *branch pruning*, to remove extraneous short branches. More details appear below on selected steps of the analysis procedure.

C. Procedure Details

Following ref. [12], let v denote the 3D image, (x, y, z) a voxel in the image, and $v(x, y, z)$ the intensity of voxel (x, y, z). The k^{th} slice (or $v(\cdot, \cdot, k)$) of v refers to all voxels having coordinate $z = k$. w_k is a working slice corresponding to $v(\cdot, \cdot, k)$ and $w_k(x, y)$ stores the temporary value of $v(x, y, k)$. A foreground (background) voxel has value $v(x, y, z) = 1$ (0). A typical micro–CT image consists of an isotropically sampled $N_x \times N_y \times N_z$ rectilinear lattice of voxels, where the sampling intervals in each direction are equal: $\Delta x = \Delta y = \Delta z = \Delta$. This isotropy permits correct application of true 3D digital image–processing operations [12].

An effective segmentation method must not only consider the image's intensity distribution, but also the spatial relationships (connectivity) of voxels constituting the regions of interest. Our proposed region–growing algorithm takes both factors into account and is a member of the class of *symmetric region-growing* algorithms [13, 15]. The essential property of a symmetric region-growing algorithm is that it will give the same segmented regions, regardless of which points in the desired segmentation are used to start it. This property gives added robustness to different initial growing conditions.

The algorithm involves two main steps: (1) 2D region growing on the individual slices and (2) region merging between consecutive slices to form complete regions. This approach enables one–pass processing. For each 2D slice, the method starts with a set of seeds that meet certain restrictive criteria. These seeded regions then grow recursively by including neighbors that satisfy loosened criteria until no further neighbors ar added. A 3D region, however, can have any shape and grow in any direction. Thus, two issues must be addressed during growing and merging. First, how should regions on consecutive slices be merged? And, second, how do regions on lower slices merge with "long past" regions on upper slices?

To solve the first issue, the method employs a *region* table and an *equivalence* table [17]. The region table stores the information on individual grown regions. This includes for each region: a *region ID*, dimensions of its *bounding–box*, *number of seeds*, and *number of pixels* (in 2D respect), acquired from 2D seeded region growing on each slice. The equivalence table contains composite information on 3D regions after merging. Each entry of the equivalence table maintains a list of region IDs of equivalent regions and other accumulated data obtained from the region table. Each entry of the region table also has a pointer linked to its corresponding entry in the equivalence table. At the end of the growing and merging process, the equivalence table is taken as the final region table.

The answer to the second issue is more complex. As the growing and merging processes progress, a (2D) region in the region table could be considered as *interesting* or *pending*, while the (3D) region in the equivalence table can be considered as *active*, *inactive*, *deletable*, or *desired*. When the growing process finishes on the first slice ($k = 0$), a 2D region can be categorized as: (1) an *interesting region* that contains seeds; (2) a *pending region* that contains no seeds but whose voxels satisfy loosened restrictions; (3) a *background region* that contains the remaining voxels. The background regions are neglected, while the information of the interesting and pending regions are stored in the region table. The merging process starts on slice k when region information becomes available on slice $(k-1)$ above it. A 3D region (in the equivalence table) is further labeled as *active* if it is involved in the merging process on the current slice or as *inactive* otherwise. The inactive 3D regions are evaluated according to other specifications: (1) minimum number of seeds in the region and (2) minimum required number of voxels in the region. After the evaluation, the inactive regions are then marked as *desired*, if they pass the specifications, or *deletable* otherwise. After the last slice ($k = N_z - 1$) is visited, every region is marked as either desired or deletable. Only the desired regions are kept as the final 3D regions.

Since the processing of a 3D image only requires one pass through the 2D slices, the visited slices are no longer used and the voxels on them can store their region numbers. Therefore, 3D seeded region growing requires only one copy of the image, plus a small amount of working buffer to maintain the region and equivalence tables. Since the main mechanism works in 2D, previously developed 2D methods can be exploited and adapted to our framework [18, 19]. A voxel looks for at most 8 neighbors for growing, instead of 26 if done in 3D. The reduction of computation time is significant, especially for huge images. When merging takes place, the overlapping (in x– and y–coordinates) portions of active regions on consecutive (k and $(k-1)$) slices are checked. Complete detail on the method appears below.

In the following description, `NumOfSeeds`(R_i) gets the number of seeds in R_i. `NumOfVoxels`(R_i) gets the number of voxels in R_i. `NumOfRegions` denotes the number of regions. Before processing, the user predefines the criteria for acceptable ROIs and how to grow the regions: $G_{seedMin}$, $G_{seedMax}$, G_{min}, G_{max}, $G_{tolerance}$, $G_{connectivity}$, $G_{leastSeeds}$, $G_{minSize}$. [$G_{seedMin}$,$G_{seedMax}$] specifies the intensity range for valid seeds. [G_{min},G_{max}] determines the allowed intensity for voxels in the final regions – no voxel outside this range will be in the final regions. Therefore, $G_{min} \leq G_{seedMin} \leq G_{seedMax} \leq G_{max}$. A voxel that is not a seed is added to an existing region if the intensity difference between it and any of its neighbors in the region is less than or equal to $G_{tolerance}$. $G_{connectivity}$ specifies the search–neighborhood sizes during growing. Please note that although $G_{connectivity}$ is specified as 26 or 6, in 3D respect, during 2D region growing, 26 is interpreted as 8 and 6 as 4, in 2D respect. The user specifies the minimum number of seeds and voxels a valid region must have using the parameters $G_{leastSeeds}$ and $G_{minSize}$. The complete algorithm appears below. Part 1 summarizes the top–level method. Parts 2 and 3 describe the lower–level stages.

1. **3D Seeded Region Growing**

   For slice $k = 0$ to $N_z - 1$.

   Perform *2D Seeded Region Growing* on slice k

If $k \geq 1$ Do *Region Merging* for slices k and $(k-1)$

For all voxels (x, y, z), $v(x, y, z) = 1$ if the region it belongs to is *desired*; otherwise, $v(x, y, z) = 0$.

2. **2D Seeded Region Growing on slice k**

(a) Initialization: Begin with voxel $(0, 0, 0)$.

(b) Find the next voxel (x, y, k) such that $G_{min} \leq v(x, y, k) \leq G_{max}$. Assign the next available region number to (x, y, k); i.e., $w_k(x, y) \leftarrow$`NumOfRegions`. `NumOfRegions`= `NumOfRegions`+1.

(c) Examine (x, y, k)'s $G_{connectivity}$ neighbors. Include the neighbor (x', y', k) recursively in a region if and only if the following predicate is `TRUE`:

$$(P1 \texttt{ AND } ((P0 \texttt{ AND } (P2 \texttt{ OR } (P3 \texttt{ AND } P4))) \texttt{ OR } (\overline{P0} \texttt{ AND } (P3 \texttt{ AND } P4))))$$

$P0 = \{v(x, y, k) \text{ in } [G_{seedMin}, G_{seedMax}]\} - (x, y, k)$ is a valid seed.

$\overline{P0} = \{v(x, y, k) \text{ not in } [G_{seedMin}, G_{seedMax}]\} - (x, y, k)$ is not a valid seed.

$P1 = \{w_k(x', y') \text{ undefined}\} - (x', y', k)$ has not been been visited yet.

$P2 = \{v(x', y', k) \text{ in } [G_{seedMin}, G_{seedMax}]\} -$ The neighbor $v(x', y', k)$ is a valid seed.

$P3 = \{v(x', y', k) \text{ in } [G_{min}, G_{max}]\} -$ The neighbor $v(x', y', k)$ is in the allowed intensity range.

$P4 = \{|v(x, y, k) - v(x', y', k)| \leq G_{tolerance}\} - v(x', y', k)$ is close enough to $v(x, y, k)$ to be added to a region.

(d) Go to 2b if more voxels on slice k still need to be examined. If not, write the values of w_k back to slice $v(\cdot, \cdot, k)$: $v(x, y, k) \leftarrow w_k(x, y)$, $\forall x, y$.

(e) Generate the following 2D region information: region ID, dimensions of the region's 2D bounding box on slice k, number of seeds, and number of voxels. The regions containing zero seeds are labeled as *pending*; otherwise, they are labeled as *interesting*.

3. **Region Merging for slice k and $(k-1)$**

(a) Locate all overlapping portions of the *active* regions between the current (k^{th}) slice and the previous ($(k-1)^{th}$) slice . A region's bounding box is used to check for overlap.

(b) Examine whether overlapping active regions should be merged. Within the overlapping portion for voxel (x, y, k) on the current slice, check its upper 5 or 9 neighbors on slice $(k-1)$, according to $G_{connectivity}$. (5 neighbors: center voxel and 4–neighbors; 9 neighbors: center voxel and 8–neighbors.) Two regions are merged if and only if the following predicate is true:

$$((P0 \texttt{ AND } (P1 \texttt{ OR } P2)) \texttt{ OR } (\overline{P0} \texttt{ AND } P2))$$

$P0 = \{v(x, y, k) \text{ in } [G_{seedMin}, G_{seedMax}]\} - v(x, y, k)$ is a valid seed.

$\overline{P0} = \{v(x, y, k) \text{ not in } [G_{seedMin}, G_{seedMax}]\} - v(x, y, k)$ is not a valid seed.

$P1 = \{v(x', y', k) \text{ in } [G_{seedMin}, G_{seedMax}]\} -$ The neighbor $v(x', y', k)$ is a valid seed.

$P2 = \{|v(x, y, k) - v(x', y', k)| \leq G_{tolerance}\} - v(x', y', k)$ is close enough to $v(x, y, k)$ to be added to a region.

(c) Update the equivalence table so that the region IDs of the merged regions are listed in the same equivalence entry. Go to 3b until all overlapping active regions have been checked.

(d) A 3D region (in the equivalence table) is labeled as *active* if it is involved in the merging process; otherwise, it is labeled as *inactive*.

(e) Evaluate 3D regions. Mark a region as *deletable* if $\texttt{NumOfSeeds}(R_i) < G_{leastSeeds}$ or $\texttt{NumOfVoxels}(R_i) < G_{minSize}$. Otherwise, mark the region as *desired*.

Region seeds correspond to bright voxels above a prespecified intensity value ($G_{seedMin}$) that form reasonably large ($G_{leastSeeds}$) connected clusters. Voxels added to the tree during growing must be locally homogeneous relative to voxels already contained in the tree (within $G_{tolerance}$) and must lie above a prespecified minimum intensity value (G_{min}). When the algorithm ends, the final outputs are: (1) an image where each voxel stores the ID of its member region; (2) a region table that contains information on all 3D regions, including whether a region is desired (set to 1) or part of the background (set to 0).

While region growing is robust, the inconsistent gray scale of the contrast medium may cause interior cavities to exist in the grown tree. Such cavities should not exist and adversely alter the tree's digital topology. 3D cavity deletion gives an extra precaution that makes the overall micro-CT analysis procedure less sensitive to scanning irregularities. The cavity deletion process performs 3D connected-component labeling on the "0" voxels; this is adapted from our 3D seeded region–growing algorithm [13, 15]. The components not adjacent to the image's outer boundary are cavities. These are filled with "1" voxels, giving a result containing a simply-connected vascular tree.

The proposed tree representation stores the skeleton of the vascular tree in a compact lossless form. It permits complete reconstruction of the original thinned image for later display. Also, it provides considerable information on the tree's structure. Our implementation traverses the skeleton image and dynamically establishes the tree–like branching structure as shown in Fig. 3a. The structure permits straightforward definitions of topological and geometrical information. It is similar to the symbolic graph-like description suggested for the cerebral vasculature by Szekely *et al.* [20].

No prior knowledge of the tree's root (generation #0) branch has yet been used to this point: the skeleton representation takes the first encountered end voxel as the root. As discussed earlier, Fig. 1a-b show that the first encountered end voxel does not necessarily belong to the root. Therefore, the tree representation of Fig. 3a does not necessarily indicate the correct branch relationships. We define the tree's root interactively. For interactive definition, the user can invoke a 3D visualization system to manually identify a root location. The tree's end voxel closest to the manually input 3D coordinates are then assigned as the root. Once the root is determined, the previously computed tree hierarchy undergoes a reorganization, as shown in Fig. 4. As this point, anatomically correct tree information, such as mother–daughter relationships and generation numbers (tree levels) are computed. Fig. 3b shows the data format for the representation.

The tree representation gives a means for straightforward computationally efficient branch pruning. (Other pruning

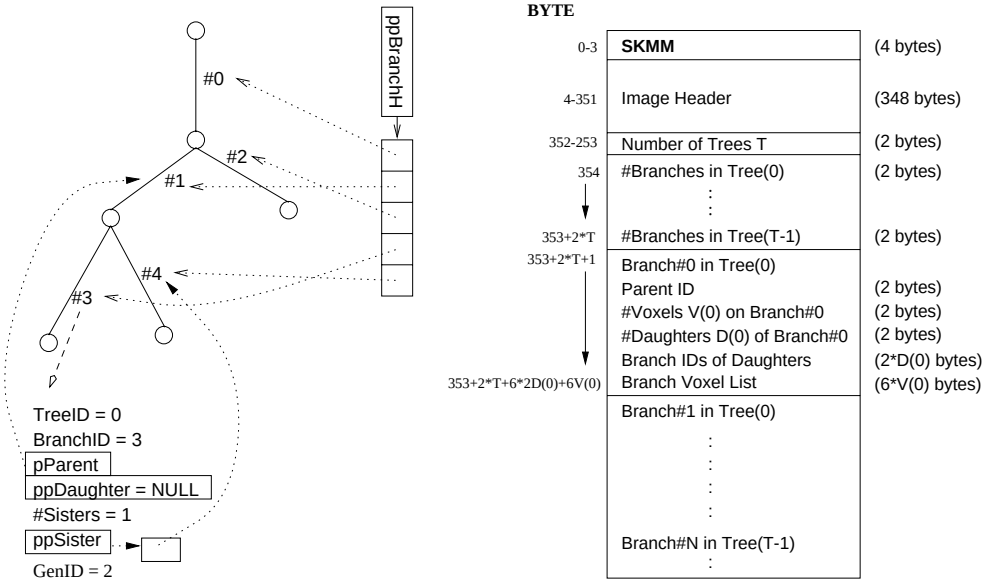

(a) Skeleton data structure. (b) File format of the tree representation

Fig. 3. Tree representation scheme. Part (a) schematically shows part of the data structure for a tree made up of three generations of branches and five total branches. The first generation starts at branch #0. The second generation consists of branches starting at the end of branch #0, etc. Branch genealogy information (parent, etc.) is also compiled at this point. Part (b) shows a small example excerpt of the complete representation. All branching, genealogy, skeleton-voxel information is captured here. The numbers indicate the computer storage required (the image header data assumes the ANALYZE header [11], but this is not required).

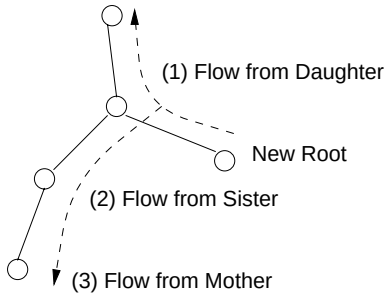

Fig. 4. Schematic illustration of Tree Reorganization. After the correct root is identified, the tree's genealogical organization is redefined. Complete tree specifications are then computed for the representation, per Fig. 3b.

approaches usually follow thinning and, hence, work on a voxel–based image [12].) Very short end branches, having no descendants, detract from interpreting the overall tree structure and often arise from digital sampling anomalies. Such branches should be pruned. A tree branch is pruned (deleted) if it has no daughter branches and if it is shorter than a prespecified minimum length. If a branch's sister is pruned, it joins with the mother branch, and the mother branch becomes longer. Affected genealogical data is updated in the tree representation. The pruning process is iterated until all branches satisfy the desired criteria.

IV. RESULTS

We first validate the automatic procedure using a mathematically constructed phantom image (Fig. 5). The original phantom consisted of 23 branches spanning 8 generations. The constructed image closely mimics the gray-scale characteristics of a typical micro-CT image. The automatic result, depicted in Fig. 5b, contains 19 branches spanning

(a) Coronal MIP image of phantom (b) Extracted branches overlaid on phantom

Fig. 5. Phantom results. The phantom was constructed using a portion of the known skeleton for *control1* (Fig. 1b). This skeleton was thickened various amounts using 3D morphological dilation to form a realistic tree. All branches were thickened an amount according to their distance from the root. Next, tree voxels were set to gray level 200. We then perform convolution with a blurring function by using a $3 \times 3 \times 3$ operator. The central voxel of the operator has 60% weight, and the other voxels are weighted 40%. Finally, additive Gaussian noise having variance $\sigma = 20$ gray levels was added, to give the final phantom image. Part (a) shows a coronal MIP image of the phantom. Part (b) depicts a coronal MIP of the phantom, with the extracted branches overlaid.

Image Name	Manual #sites	Auto #sites	Error Measures				
			Mean	Dev	Max x	Max y	Max z
phantom	514	495	1.013	1.010	1.500	1.200	1.100
control1	544	525	1.888	1.676	5.000	3.000	12.330
control2	271	298	1.592	1.014	5.750	2.900	4.080
control3	252	225	3.481	1.903	4.090	4.730	6.420

Fig. 6. Numerical comparison between known and automatically computed branch measurements. The phantom results give averages over all branches found automatically. The liver-image results consider one manually defined path and the corresponding automatically defined path. "Mean" indicates the mean coordinate difference between sites on an manually defined path and an automatically defined path. "Dev" equals the standard deviation of "Mean." "Max x" is the maximum x–coordinate difference over all sites on a manually defined path and an automatically defined path. "Max y" and "Max z" denote similar measures for y– and z–coordinate differences.

7 generations; a short branch near the middle of the phantom image was removed, causing the number of extracted branches and generations to be fewer than the original. Fig. 6 gives a numerical comparison between the actual known skeletal branches and the automatically defined branches. The results show a strong correlation, with average tree-voxel positional differences on the order of 1 voxel.

We next give results for the rat liver images of Fig. 1. Manual traces of a single path, extending from the root to a terminating branch, were done previously for these images. Because of excessive interaction time, it was not feasible to extract more branches manually. The automated procedure, on the other hand, extracts complete trees. The numerical and visual results of Figures 6-11 demonstrate our procedure's efficacy. While many branches are extracted, Figures 7-9 may seem to indicate that even more could be defined. By relaxing the region-growing parameters and the pruning process, more branches could be extracted. However, many of these branches have poor initial gray-level definition. Hence, their value is unclear. Note that *control3* (Figure 10(c)) actually shows a partial second tree "artifactually" connected to the periphery of the main tree. This may be an artifact or it could conceivably be a true collateral arterial connection. The gray-scale similarities and sample spacing of the image data make it difficult to positively know which conclusion is correct. Also note that the surface rendering of Figure 10 shows segmented trees before tree representation. The trees, as shown by superimposed paths in Figures 7-9, indicate the actual preserved branches. By pruning the tree based on generation index, the artifactual tree depicted in the rendering of Figure 10c

(a) Automatically extracted tree (b) One automatically extracted path comparable to (c) (c) Manually traced path

Fig. 7. Coronal MIP images of a 3D rat liver *control1*, with extracted biliary tree overlaid. For the automatically extracted paths, the parameters of each module are as follows. 3D seeded region growing: $G_{seedMin} = 120, G_{min} = 80, G_{tolerance} = 10, G_{leastSeeds} = 5$, Root Identification: approximate root = $(64, 75, 488)$, computed root = $(73, 70, 472)$. Branch pruning criteria: a tree has at least 10 branches and has at least 30 voxels; each branch has at least 20 voxels.

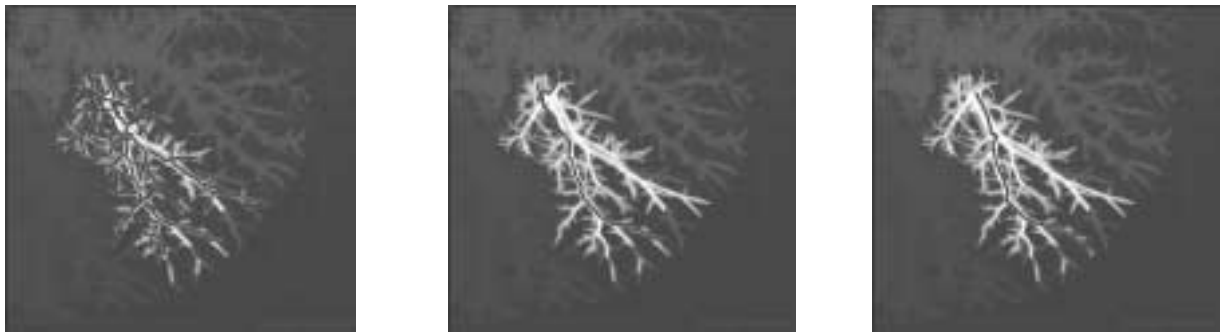

(a) Automatically extracted tree (b) One automatically extracted path comparable to (c) (c) Manually traced path

Fig. 8. Coronal MIP images of a 3D rat liver *control2*, with extracted biliary tree overlaid. For the automatically extracted paths, the parameters of each module are as follows. 3D seeded region growing: $G_{seedMin} = 230, G_{min} = 180, G_{tolerance} = 10, G_{leastSeeds} = 5$, Root Identification: approximate root = $(114, 205, 274)$, computed root = $(117, 204, 274)$. Branch pruning criteria: a tree has at least 10 branches and has at least 30 voxels; each branch has at least 20 voxels.

does not contribute to the final tree representation as shown in Figure 9b. Fig. 11 shows that our tree representation is more storage–efficient than even a gzipped thinned image (gzip is a standard UNIX-based file-compression technique). Fig. 12 gives a breakdown of processing time on a PC for the liver images. The times for region growing and tree manipulation account for only a few percent of the total time.

V. Discussion

The results of this paper show that the proposed automated procedure is practical to run on current PCs. The procedure is memory–efficient and provides a comprehensive representation of the extracted tree. When loading a micro–CT image during processing, the memory is allocated slice by slice. Therefore, a partial image can be loaded; thus, by exploiting the xyz–separable characteristics of our methods, the requirement for processing memory may be further reduced. The greatest advantage of our procedure is its ability to extract a large complex tree. The large size of the micro-CT images makes operator–based definition of the tree essentially impossible. Further, we believe that the computer-based methods should more accurately extract single branches than the human. This is because the

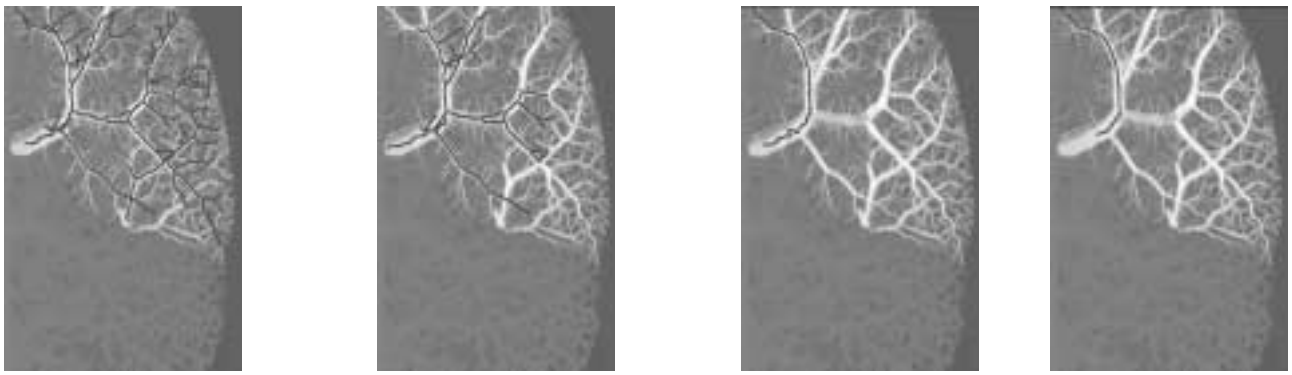

(a) Auto-extracted tree (b) Pruned (a) by generation index (c) One path from (a) comparable to (d) (d) Manually traced path

Fig. 9. Coronal MIP images of 3D rat liver *control3*, with extracted biliary tree overlaid. For the automatically extracted paths, the parameters of each module are as follows. 3D seeded region growing: $G_{seedMin} = 200, G_{min} = 130, G_{tolerance} = 10, G_{leastSeeds} = 5$, Root Identification: approximate root = $(13, 165, 292)$, computed root = $(28, 92, 303)$. Branch pruning criteria: a tree has at least 10 branches and has at least 30 voxels; each branch has at least 20 voxels. Reference [14] gives complete detail on the parameters.

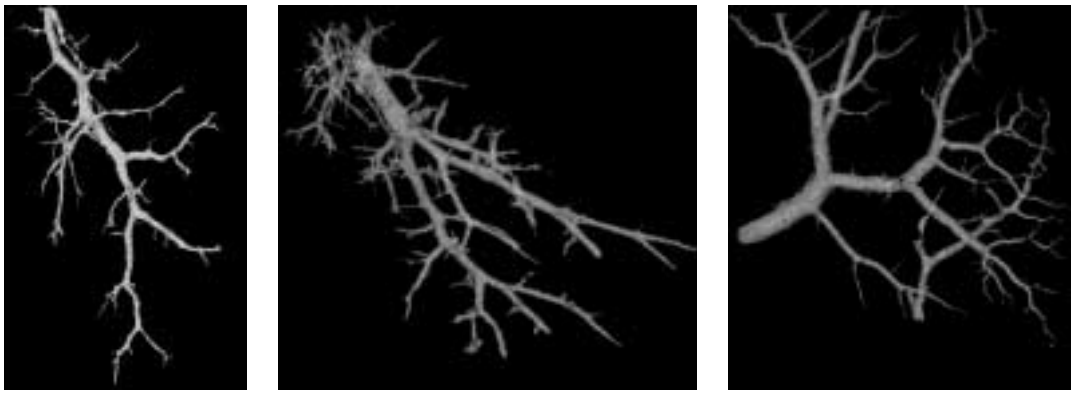

(a) *control1* (b) *control2* (c) *control3*

Fig. 10. 3D surface renderings of extracted vascular trees.

Image Name	Tree Data		Storage Requirements			
	#br	#gen	size	thin	gzip	tree
control1	51	14	80.2MB	40.1MB	52KB	9KB
control2	15	6	114.4MB	57.2MB	65KB	13KB
control3	69	12	73.0MB	36.5MB	44KB	18KB

Fig. 11. Profile of automated results for the rat livers. #br and #gen denote numbers of branches and generations extracted by the automatic procedure. The storage requirements indicate the how much storage a particular form uses; "size" denotes the original 3D image, "thin" denotes the image after 3D thinning, "gzip" is a gzipped version of the thinned image, and "tree" is our proposed tree representation.

Image Name	Image Size	Time usage (in seconds)						
		sig	seg	cav	thin	rep	man	total
control1	80.2MB	104	8	69	121	6	$\ll 1$	**309**
control2	114.4MB	147	9	98	6	8	$\ll 1$	**269**
control3	73.0MB	95	8	64	291	5	$\ll 1$	**464**

Fig. 12. Running time usage on a PC (Windows NT, CPU 400MHz). sig={Sigma Filter}; seg={3D seeded region growing}; cav={cavity deletion}; thin={thinning}; rep={Skeleton representation}; man={Skeleton manipulation: Root Identification, Tree Reorganization, Pruning.}.

methods draw upon the true 3D topological properties of the image data.

The procedure is, for the most part, generically applicable to large 3D isotropic 16-bit images containing large, bright, tree-like structures (we have also applied it to 3D rat cardiac micro-CT images and 3D CT human-liver images [14, 21]). The main parameters that need adjusting are those in seeded region growing. All processing beyond region growing does not depend on the image's gray-scale characteristics and is, hence, generally applicable in all circumstances involving large 3D trees.

The branching geometry of vascular trees reflects the several physiological mechanisms which control vessel diameters and branching angles and the physical constraints placed on the organ shape. Examples of three different branching geometries are the hepatic (little shape constraint), the pulmonary (with constraints imposed by the airways) and the coronary (with epicardial surface constraints). These constraints, plus any differences in the remodeling of those branching geometries in response to pathological factors (e.g., hypertension), should impact on the spatial distribution of blood flow and the limits of flow reserve. The role of the branching geometry can be adequately understood only if the accurate and complete branching structure is quantitated. For this reason, the automated methodology is essential because of its consistency, accuracy and speed. The computed tree representation provides an extensive source of information to analyze the geometric characteristics of the hepatic vasculature and other vascular beds; we have begun a preliminary study along this line for the coronary microvasculature captured in micro-CT images of rat hearts [21]. More suitable interactive visualization and editing tools can also be used to perform such studies [15].

Acknowledgments

This work was partially supported by NIH grants # R01-RR11800 and # R01-CA74325, by the Whitaker Foundation, and by NSF grant # BIR-9317816 under the Instrument Development for Biological Research Program. The manually analyzed results were generated by Patricia E. Lund and Catherine A. Seaman. A preliminary version of this work appeared at an unreviewed conference [14]. The rats studied were part of a bile duct study performed by Dr. Nicholas LaRusso of the Mayo Clinic, Department of Internal Medicine and funded by NIH grant # DK24031.

References

[1] B. P. Flannery, H. W. Deckman, W. G. Roberge, and K. L. D'Amico, "Three-dimensional x-ray microtomography," *Science*, vol. 237, pp. 1439–1444, 1987.

[2] F. Peyrin, J.-P. Houssard, E. Maurincomme, G. Peix, R. Goutte, A.-M. Laval-Jeantet, and M. Amiel, "3D display of high resolution vertebral structure images," *Computerized Medical Imaging and Graphics*, vol. 17, no. 4/5, pp. 251–256, 1993.

[3] M. E. Casey, L. Eriksson, M. Schmand, M. S. Andreaco, M. Paulus, M. Dahlbom, and R. Nutt, "Investigation of LSO crystals for high resolution positron emission tomography," *IEEE Transactions on Nuclear Science*, vol. 44 (Part 2), pp. 1109–1113, June 1997.

[4] S. M. Jorgensen, O. Demirkaya, and E. L. Ritman, "Three dimensional imaging of vasculature and parenchyma in intact rodent organs with x–ray micro–CT," *Am J. Physiol (Heart, Circ Physiol 44)*, vol. 275, pp. H1103–H1114, 1998.

[5] R. H. Johnson, H. Hu, S. T. Haworth, P. S. Cho, C. A. Dawson, and J. H. Linehan, "Feldkamp and circle-and-line conebeam reconstruction for 3D micro-CT of vascular networks," *Physics in Medicine and Biology*, vol. 43, no. 4, pp. 929–940, 1998.

[6] H. Benveniste, H. Qiu, L. Hedlund, P. Huttemeier, S. Steele, and G. Johnson, "In vivo diffusion-weighted magnetic resonance microscopy of rat spinal cord: effect of ischemia and intrathecal hyperbaric 5% lidocaine," *Regional Anesthesia and Pain Medicine*, vol. 24, no. 4, pp. 311–318, 1999.

[7] High Resolution Imaging in Small Animals with PET, MR and Other Modalities, Amsterdam September 27-29, 1999. URL: http://www-HiRes.cc.nih.gov/HiRes.

[8] E. L. Ritman, S. M. Jorgensen, P. E. Lund, P. J. Thomas, J. H. Dunsmuir, J. C. Romero, R. T. Turner, and M. E. Bolander, "Synchrotron-based micro-CT of in situ biological basic functional units and their integration," in *Proceedings of SPIE Medical Imaging 1997: Physiology and Function from Multidimensional Images*, vol. 3149, pp. 13–24, 1997.

[9] A. Garcia-Sanz, A. Rodriguez-Barbero, M. D. Bentley, E. L. Ritman, and J. C. Romero, "Three-dimensional microcomputed tomography of renal vasculature in rats," *Hypertension*, vol. 31, no. Part 2, pp. 440–444, 1998.

[10] P. E. Lund, C. A. Seaman, and E. L. Ritman, "3D branching geometries of epicardial and intra-myocardial coronary arteries in 3 to 25-week old rats," *American Jounal of Physiology (Heart, Circulatory Physiology)*, In Review 1999.
[11] R. A. Robb, *Three-Dimensional Biomedical Imaging: Principles and Practice*. New York: VCH Publishers, 1994.
[12] W. E. Higgins, R. A. Karwoski, W. J. T. Spyra, and E. L. Ritman, "System for analyzing true three-dimensional angiograms," *IEEE Transactions on Medical Imaging*, vol. 15, pp. 377–385, June 1996.
[13] S.-Y. Wan and W. Higgins, "Symmetric region growing," *IEEE International Conference on Image Processing (ICIP2000)*, to appear 2000.
[14] S.-Y. Wan, E. L. Ritman, and W. E. Higgins, "Extraction and analysis of large vascular networks in 3D micro-CT images," in *Proceedings of SPIE Medical Imaging 1999: Physiology and Function from Multidimensional Images*, vol. 3660, pp. 322–334, A. Clough and C.T Chen, eds., 1999.
[15] S.-Y. Wan, "Analysis and visualization of large branching networks in 3-D digital images," *Ph.D. Dissertation, Dept. Computer Science and Engineering, The Pennsylvania State University*, August 2000.
[16] P. K. Saha, B. B. Chaudhuri, and D. D. Majumder, "A new shape preserving parallel thinning algorithm for 3D digital images," *Pattern Recognition*, vol. 30, no. 12, pp. 1939–1955, 1997.
[17] R. Jain, R. Kasturi, and B. G. Schunck, *Machine Vision*. New York: MIT Press and McGraw-Hill Inc., 1995.
[18] R. M. Haralick and L. G. Shapiro, "Survey: Image segmentation techniques," *Computer Vision, Graphics and Image Processing*, vol. 29, pp. 100–132, January 1985.
[19] Y.-L. Chang and X. Li, "Adaptive image region-growing," *IEEE Transactions on Image Processing*, vol. 3, pp. 868–872, November 1994.
[20] G. Szekely, T. Koller, R. Kikinis, and G. Gerig, "Structural description and combined 3-D display for superior analysis of cerebral vascularity from MRA," in *Proc. SPIE*, vol. 2359, pp. 272–281, 1994.
[21] S.-Y. Wan, P. E. Lund, D. A. Reyes, C. A. Seaman, W. E. Higgins, and E. L. Ritman, "Heterogeneity of coronary arterial branching geometry," in *Proceedings of SPIE Medical Imaging 2000: Physiology and Function from Multidimensional Images*, vol. 3978, pp. 515–520, A. Clough and C.T Chen, eds., 2000.